Phenol photocatalytic degradation over anisotropic TiO₂ nanomaterials: Kinetic study, adsorption isotherms and formal mechanisms

Asma Turki [a], Chantal Guillard [b], Frédéric Dappozze [b], Zouhaier Ksibi [a], Gilles Berhault [b], Hafedh Kochkar [a,c,*]

[a] Université de Tunis El Manar, Faculté des Sciences de Tunis, Laboratoire de Chimie des Matériaux et Catalyse, 2092 Tunis, Tunisia
[b] Institut de Recherches sur la Catalyse et l'Environnement, IRCELYON, CNRS—University of Lyon, Villeurbanne 69100, France
[c] Laboratoire de Valorisation des Matériaux Utiles, Centre National de Recherches en Sciences des Matériaux (CNRSM), Technopôle Borj-Cédria, 8027 Soliman, Tunisia

ARTICLE INFO

ABSTRACT

Anisotropic TiO₂ nanomaterials (nanotubes, nanorods, nanoplates, nanospheres, and nanoparticles) with controlled structural and textural properties have been evaluated in the photocatalytic degradation of phenol under UV conditions. The kinetic study of phenol adsorption fits well to a quasi-second-order model whereas the adsorption isotherms of phenol over the different TiO₂ nanomaterials follow the Langmuir model and the degradation kinetics the Langmuir–Hinshelwood (L–H) model. TiO₂ nanomaterials exposing (0 0 1) or (1 0 1) anatase facets are less active than TiO₂ P25 for the phenol degradation. This is related to their tendency to degrade faster intermediates products (organic acids) rather than phenol itself. A good compromise between anatase crystallinity, crystallites sizes, and specific surface area can however improve the photocatalytic activity of the TiO₂ nanomaterials. Results also showed that the degradation mechanism follows pseudo-first order kinetics. Pseudo-rate constants were therefore determined and formal mechanism schemes proposed.

© 2014 Elsevier B.V. All rights reserved.

1. Introduction

The contamination of natural and drinking water supplies and of the aquatic environment has become nowadays a serious environmental problem worldwide [1–6]. Wastewater treatment is based upon various mechanical, biological, physical, and chemical processes. In fact, this is a combination of many conventional operations like coagulation, sedimentation, precipitative softening, filtration, and chlorination of effluents polluted by organic pollutants [7,8]. After elimination of the particles in suspension, the biological treatment remains the ideal process for wastewater treatment, particularly at low pollutant concentrations. Nevertheless, some organic pollutants are not biodegradable and are known as Bio-Recalcitrant Organic Compounds (BROC). Despite their low concentration, these contaminants are a major health concern because of their extremely high endocrine disrupting potency and genotoxicity [9–11]. Therefore, the effective removal of BROC from wastewater effluent is of high interest.

Many technologies based on Advanced Oxidation Processes (AOPs) have been used to overcome this critical problem [12–15]. AOPs processes are based on the generation of strongly oxidizing hydroxyl radicals ($HO^\bullet$), which in turn are able to degrade the most recalcitrant molecules into biodegradable compounds. Heterogeneous photocatalysis [16–18] was found to be one of the most promising AOPs for wastewater treatment due to the mild operating conditions, the wide spectrum of pollutants able to be degraded and to its high efficiency for complete organic compounds mineralization to carbon dioxide and water. Using the photocatalysis process, recalcitrant organics are degraded by the combined actions of mainly: (i) a semiconductor photocatalyst, (ii) an energetic radiation source (an artificial or natural light) and (iii) an oxidizing agent [19–21]. Metal oxides and sulfide materials represent a large class of semiconductors suitable for photocatalysis. In particular,

* Corresponding author at: Laboratoire de Valorisation des Matériaux Utiles, Centre National de Recherches en Sciences des Matériaux (CNRSM), Technopôle Borj-Cédria, 8027 Soliman, Tunisia. Tel.: +216 79 325 250; fax: +216 79 325 314.
E-mail addresses: asmaturki@gmail.com (A. Turki), h_kochkar@yahoo.fr (H. Kochkar).

titanium dioxide has been widely employed [22–24], thanks to its outstanding photocatalytic activity, ready availability, low toxicity, inertness, low costand high stability compared to other semiconductors. Moreover, TiO$_2$ shows high efficiency in the complete mineralization of various toxic and bio-recalcitrant organic compounds such as organochloride compounds [25–27], organic acids [28–30], pesticides [31], herbicides [32], and dyes [33].

Phenolic compounds are major pollutants of the aquatic environment due to their widespread use in agricultural, petrochemical, textile, paint, plastic, and pesticidal chemical industries. They are well known to be biorecalcitrant and to have acute toxicity with carcinogenic and mutagenic characters [34,35]. According to the environmental protection rules of the Central Pollution Control Board, the discharge limits of phenols in inland water must not exceed a concentration of 1 mg L^{-1} [34]. For this reason, the photocatalytic degradation of phenol or substituted phenols in wastewater by the TiO$_2$/UV process has been widely investigated [36–39].

Although heterogeneous photocatalysis appears in numerous forms, the photocatalytic degradation of phenol and substituted phenols in wastewater has recently been the most widely investigated in several reviews [40,41]. Information from various investigations suggests that the photocatalytic degradation of phenol and its derivatives is mainly dependent on the solution pH, catalysts and their composition, organic substrate type and concentration, light intensity, catalyst loading, ionic composition of waste water, types of solvent, oxidant concentration, and calcination temperatures. Understanding the impacts of various parameters on the photocatalytic degradation efficiency is of paramount importance from the design and operational points of view when choosing a sustainable, efficient technique for the treatment of waste water. The assessment of the different behavior of TiO$_2$ nanomaterials is difficult because they have not been prepared or tested in a similar way to be comparable

Using the TiO$_2$/UV process, several parameters were found to influence the photocatalytic degradation of phenol [34,42,43] such as: the pH of the solution, the concentration of TiO$_2$, the initial concentration of phenol, the presence of anions, the presence of metal ions, the type and concentration of electron acceptors (O$_2$, H$_2$O$_2$) and the intensity of the UV light. However, other factors were more recently found to play a key role in the photocatalytic efficiency in general: the content of the anatase phase and its crystallinity [44–46], the type of exposed crystalline planes [47], the crystallite size and the presence of structural defects [38,48], the morphology and specific surface area [49]. Indeed, according to the literature, anatase is the most active allotropic TiO$_2$ form among others like brookite, rutile, and TiO$_2$(B). Better photocatalytic activity would be reached when the (101) plane of anatase is preferentially exposed [47]. Araña et al. [38] and Liu et al. [48] showed that in order to decrease the recombination rate, structural defects must be minimized through an optimization of the crystallite size of TiO$_2$. A recent review by Nakata et al. [49] shows the relationship between the morphology or "design" of TiO$_2$ nanomaterials with controlled properties and intended applications. In fact, 1D-TiO$_2$ nanomaterials, such as fibers and tubes, possess a higher surface-to-volume ratio yielding to a reduction in the hole–electron recombination rate and therefore to higher interfacial charge carrier transfer rate.

In the present study, we will focus on the photocatalytic degradation of phenol over anisotropic TiO$_2$ nanomaterials presenting different shapes like: nanotubes, nanowires, nanorods, and nanoparticles.

The phenol adsorption kinetic model and isotherms will be discussed and correlated to the structural, textural, and morphological properties of TiO$_2$ nanomaterials. The intermediate products will be determined and quantified while mineralization tests will be performed in order to better ascertain the photodegradation formal mechanism. Finally, the effect of pH on the photocatalytic properties will be discussed.

2. Experimental

2.1. Materials and reagents

Titanate nanotubes (HTNT) were prepared via alkaline hydrothermal treatment [50]. Typically, 3.0 g of TiO$_2$ powder (P25) were treated with 90 mL of a concentrated solution of NaOH (11.25 M) in a 150 mL Teflon-lined autoclave at 130 °C for 20 h. The resulting precipitate was separated by filtration and washed twice with HCl solution (Panreac Quimica SA, 37%) of 0.1 mol L^{-1} and 1 mol L^{-1} respectively and ultra-pure hot water in order to remove sodium. Finally, the HTNT material was calcined from 400 to 700 °C in air for 2 h. The calcined materials are named HTNT-T with T is the calcination temperature.

Titanates nanowires (HTNW) were elaborated following the same protocol used for nanotubes except that a concentrated solution of KOH (12.5 M) was used instead of NaOH, while operating conditions were 155 °C for 24 h [51–53]. Similar washing steps as used for HTNT with ultra pure water and HCl solutions were conducted in order to remove potassium. The resulting material is named HTNW. Finally, the HTNW material was calcined at 700 °C in air for 2 h. The calcined material is therefore named HNTW-700. We have chosen this calcination temperature (700 °C) by referring to the work of Jitputti et al. [54] who have found the formation of a pure well-crystallized anatase phase.

The elaboration of TiO$_2$ nanorods (TNR) was performed through a hydrothermal treatment of titanate nanotubes (2.0 g) in the presence of ultrapure water (120 mL). The hydrothermal treatment was carried out at 200 °C for 24 h [52,53].

All the chemicals and reagents used in the present study were analytical and HPLC grade. Phenol, catechol, maleic acid, fumaric acid, propionic acid, acetic acid, tartaric acid, and succinic acid were obtained from Aldrich. 1,4-benzoquinone and hydroquinone were purchased from Fluka, and formic acid from Acrōs Organics. NaOH and HNO$_3$ were purchased from Fisher Chemicals (98%) and Merck KGaA (65%) respectively. Phenol and standard solutions were prepared using purified water (18 MΩ cm) obtained from Millipore Waters Milli-Q apparatus.

2.2. Adsorption and photocatalytic experiments

The magnetically stirred aqueous suspensions (phenol/TiO$_2$ photocatalyt) were UV-A irradiated in a Pyrex cylindrical flask (total volume ca. 100 mL) at atmospheric pressure, with a bottom optical window of ca. 4 cm diameter. The radiant flux was provided by a Philips HPK 125 W mercury lamp which provides maximum energy at 365 nm. An optical filter Corning 0.52 was installed to cut off wavelengths below 340 nm. A 2.2 cm circulating-water cell was used to remove IR radiation in order to prevent any heating of the suspension. The radiant flux was measured with a VLX-3W radiometer with a CX-365 detector (UV-A). The distance "d" which separates the photoreactor from the water cell is regulated all time in order to preserve the radiant flux constant at 5.0 ± 0.2 mW cm^{-2} for all photocatalytic tests. For each experiment, 30 mg of photocatalyst was added to 30 mL of phenol solution and stirred in the dark for 30 min for kinetic adsorption measurements. The photocatalytic degradation was carried out at room temperature and at natural pH (ca. 6.0 ± 0.2). In order to study the adsorption phenomenon and the photodegradation kinetics, different concentrations of phenol were used (from 5 to 400 mg L^{-1}). At different times of photoreaction, samples were filtered using a 0.45 μm Millipore filter to remove TiO$_2$ particles before analysis.

2.3. Characterization

Low temperature nitrogen adsorption measurements were done using a Micromeritics ASAP 2020 instrument. The Brunauer–Emmett–Teller (BET) specific surface areas (S_{BET}) were determined by a multipoint BET method using the adsorption data in the relative pressure P/P_0 range of 0.05–0.25. The nitrogen adsorption volumes at the relative pressure (P/P_0) of 0.95 were used to determine the total pore volumes.

The phase identification of the sample was done by X-ray Diffraction (XRD) analyses using a Bruker D8 Advance A25 diffractometer with Cu-Kα radiation ($\lambda = 1.54184$ Å). The "HighScore Plus" software was used for the identification of phases.

The morphology of the different samples was studied by Transmission Electron Microscopy (TEM) and High Resolution TEM (HRTEM) using a JEOL 2010 instrument operating at 200 kV. The microscope was equipped with an ultrahigh-resolution polar piece (point resolution: 1.9 Å). The specimens for TEM analysis were prepared by dropping and drying the colloidal solution onto a holey carbon film supported on a Cu grid (300 mesh).

2.4. Analytical measurements

The concentrations of phenol and intermediates were determined by HPLC (Supplementary data Table T1). HPLC analyses were performed using VARIAN ProStar system with a diode array and with a 125 mm × 4 mm C18 reverse-phase column (Agilent Technologie) to follow the Phenol degradation and aromatic intermediates formation. The mobile phase composition was methanol and water acidified with phosphoric acid (pH 3.0) at a volume ratio of 5:95. However, for organic acid intermediates, the HPLC analyses were performed using VARIAN ProStar system with a single wavelength UV–Vis detector equipped with 300 mm × 7.8 mm carbohydrate analysis column (COREGEL-87H3). The mobile phase was an H_2SO_4 solution (5.10^{-3} mol L^{-1}) and the flow rate was set to 0.7 mL min^{-1}. The detection wavelength was set at 210 nm.

The mineralization percentage of phenol was determined through the Total Organic Carbon (TOC) content. TOC was measured with a Shimadzu model TOC-Control V equipped with an autosampler and calibrated with standard solutions of potassium hydrogen-phthalate. Under these conditions, the detection limit of the TOC analyzer is 0.1 mg L^{-1} and the quantification limit is 0.5 mg L^{-1}.

3. Results and discussion

3.1. Characterization of the different TiO_2 nanomaterials

The following paragraph summarizes the main characteristics of the different TiO_2 nanomaterials studied here. A more complete characterization analysis is described elsewhere [50,52,53]. TEM micrographs of HTNT and HTNT-400 are shown in Fig. 1. HTNT appears as a multiwalled nanotubular structure with a length of 100–300 nm, an outer diameter of 10–14 nm and a wall thickness of 2–3 nm (Fig. 1A). After post-treatment, HTNT-400 preserves the nanotubular morphology (Fig. 1B) with open ends (Fig. 1C) and with an interlayer spacing of 0.35 nm corresponding to the (1 0 1) plane of anatase (Fig. 1D). After calcination at 500 °C, HTNT-500 (Fig. 1E) loses completely its nanotubular morphology leading to the formation of nanoplates with length of 50–70 nm and thickness of around 10 nm. After calcination at 600 °C (Fig. 1F), the nanoplate morphology is not observed anymore and only aggregated nanoparticles are obtained.

HTNW presents fibrous nanowire morphology of several hundred nanometers in length with a small diameter (7–12 nm)
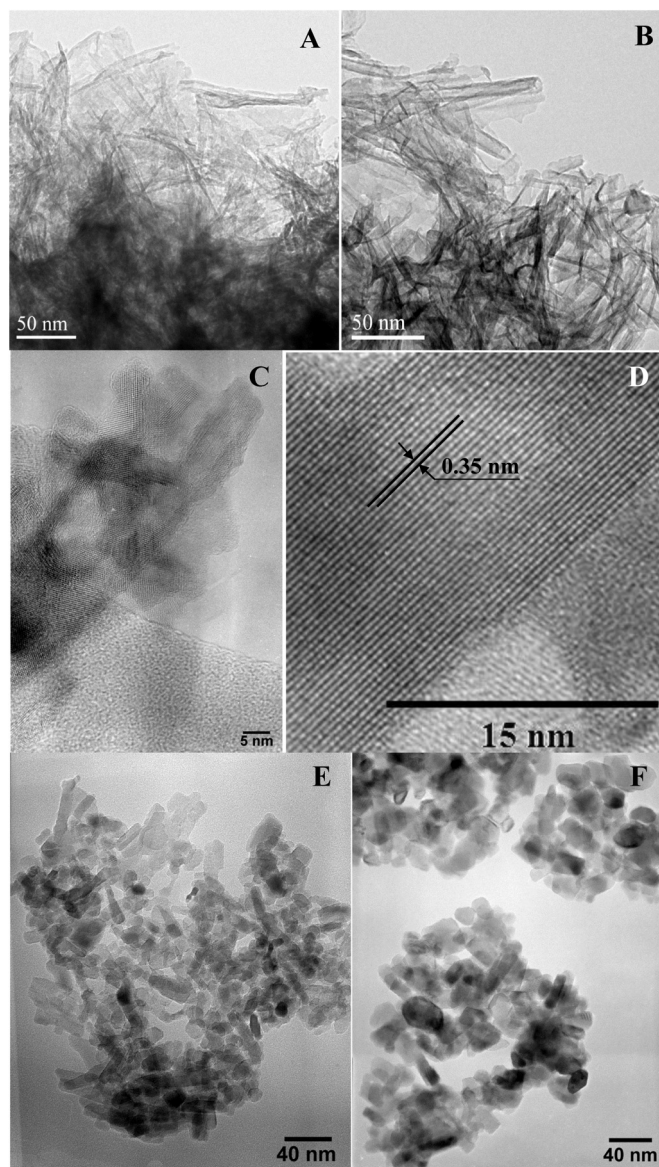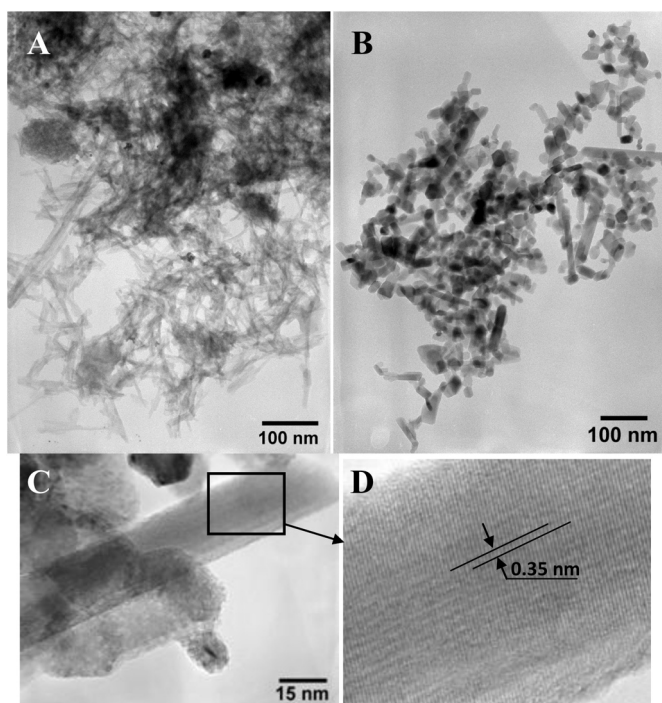

Fig. 1. TEM micrographs of the as-elaborated HTNT material (A) and HTNT-400 material (B, C); HRTEM image on the extremity of one of the nanotubes of the HTNT-400 sample (D); TEM micrographs of HTNT-500 (E) and HTNT-600 (F) materials.

(Fig. 2A). Nanowires present a rough surface aspect. Upon calcination at 700 °C nanowires are transformed into nanorods and nanoparticles (Fig. 2B). Nanorods are present in a lower proportion than nanoparticles. Nanorods diameter are 20–40 nm with a length of 130–280 nm. HRMET micrograph of HTNW-700 shows clearly the fingerprint of (1 0 1) plane of anatase phase ($d_{(1 0 1)} \approx 0.3$ nm) (Fig. 2C-D).

TEM micrographs in Fig. 3 show that TNR exhibits a spindle-like morphology corresponding to nanorods with an oval shape. These spindle-like particles have length of ca. 100–200 nm and a 30–60 nm diameter. Up to our knowledge, this spindle-like morphology has been rarely observed up to now using hydrothermal techniques [55,56]. Peng et al. [55] obtained anatase TiO_2 nanocrystals with a rice-like aspect through a hydrothermal treatment of Ti(OH)$_3$ in deionized water. Li et al. [56] also obtained rice-like nanoparticles using a hydrothermal treatment of titanate nanowires but only through the addition of a structuring agent, cetyltrimethylammonium bromide. Besides these spindle-like nanorods, cubic nanoparticles are also observed (Fig. 3A–B).

Fig. 2. TEM micrographs of the as-elaborated HTNW material (A) and HTNW-700 material (B, C); Zoom on one of the nanorod of the HTNW-700 sample (D).

only but this material exhibits a higher crystallization with respect to HTNW-700 and HTNT-400.

The transformation of TiO$_2$ P25 into HTNT or HTNW is accompanied by the formation of hydrogenotitanate materials showing very high specific surface areas (Table 1) with values respectively of 308 m^2/g and 375 m^2/g for HTNT and HTNW. Post-thermal treatment of HTNT nanomaterials leads simultaneously to a severe decrease of the surface area and pore volume. After calcination at 400 °C, the surface area of HTNT-400 decreases to 174 m^2/g. Further treatment at higher temperatures leads to an even more drastic decrease with only 30 m^2/g for HTNT-700. Calcination of HTNW to 700 °C also leads to a severe loss in specific surface area (50 m^2/g). Moreover, pore volumes tend to decrease with the post-thermal treatment in a similar fashion than surface areas. Once again, HTNW-700 presents a higher pore volume than HTNT-700 (0.31 cm^3 g^{-1} vs 0.16 cm^3 g^{-1}) showing a better stability of nanowires with respect to nanotubes.

3.2. Phenol adsorption kinetics

TiO$_2$ nanotubes, nanowires, and nanoparticles present different adsorption sites [59,60]. The nature and the number of these sites will define the adsorption ability of each catalyst. In order to analyze the adsorption process of phenol, two models were tested to fit the adsorption curve namely: a quasi-first-order adsorption rate equation (model Lagergren) [61] and a quasi-second-order adsorption rate equation (model Ho and McKav) [62].

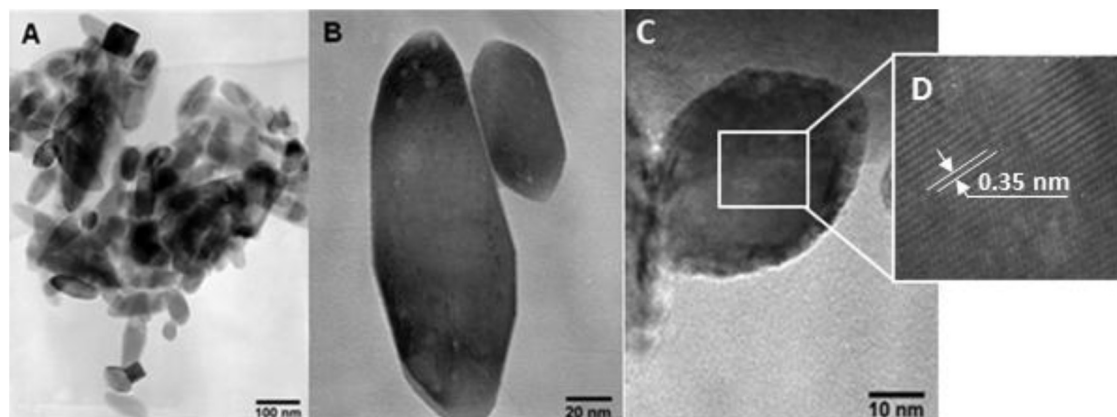#### 3.2.1. Fit using the quasi-first-order kinetic model

The quasi-first-order kinetic equation is also known as the quasi-first-order rate equation or the Lagergren quasi-first-order kinetic equation. This model is based on the assumption that the adsorption rate is determined by the number of adsorption sites on the surface of the adsorbent (Eq. (1)) [61].

$$\frac{dQ_t}{dt} = k_1.(Q_e - Q_t) \qquad (1)$$

where Q_t and Q_e are the amounts of phenol at time t and at equilibrium (mg g^{-1}), respectively and k_1 is the quasi-first-order rate constant (min^{-1}). The integration of Eq. (1) gives:

$$\log(Q_e - Q_t) = \log(Q_e) - \frac{k_1}{2.303}t \qquad (2)$$

The R^2 values for the quasi-first-order kinetic equations fitted for different TiO$_2$ nanomaterials (not shown here) are all lower than 0.5 with no regular variation. Therefore, the adsorption of phenol into TiO$_2$ nanomaterials does not meet quasi-first-order kinetic adsorption process.

HRMET micrograph of TNR shows clearly the fingerprint of (1 0 1) plane of anatase phase ($d_{(1 0 1)} \approx 0.35$ nm) (Fig. 3D). Table 1 summarizes the morphologies observed for the different samples studied by TEM.

Composition and structure were also analyzed by XRD and elemental analysis (Table 1 and Supplementary data Fig. S1). The XRD patterns of HTNT and HTNW correspond to an orthorhombic hydrogenotitanate phase of the type M$_x$H$_{2-x}$Ti$_2$O$_5$·H$_2$O (M = Na or K) [50]. Elemental analysis reveals that after acid washing, HTNT and HTNW are free of alkali ions. After calcination at 400 °C, the diffractogram of HTNT-400 corresponds only to the anatase phase. The diffraction peaks observed at $2\theta = 9.8°$ for the initial HTNT is characteristic of the interlayer distance between nanotube walls [57]. This peak shifts to a higher 2θ value (14.0°) after calcination showing a contraction of the interlayer distance due to dehydration occurring during the titanate-anatase transformation [58]. After calcination at 700 °C, HTNW-700 gives rise only the anatase diffraction peaks. Similarly, the TNR diffractogram corresponds to anatase


Fig. 3. TEM micrographs of the TNR material at different magnifications (A–C). Zoom on one of rice-shaped TNR sample (D).

Table 1
Textural, morphological, and structural properties of TiO$_2$ nanomaterials.

Photocatalysts	Morphologies (TEM)	Crystalline structure (XRD)	S_{BET} (m^2 g^{-1})	V_{meso} (cm^3 g^{-1})	E_g (eV) ± 0.05 eV
HTNT	Nanotubes	H$_2$Ti$_3$O$_5$·H$_2$O (poorly crystalline)	308	0.64	3.31
HTNT-400	Nanotubes $D_{ext} \approx$ 10 nm, $D_{int} \approx$ 4 nm, $L \approx$ 100–300 nm	Anatase (poorly crystalline) L_{hkl} = 10 nm	174	0.58	3.17
HTNT-500	Mixture of nanoparticles and nanorods $D_{ext} \approx$ 10–30 nm	Anatase (highly crystalline) L_{hkl} = 14 nm	107	0.46	3.19
HTNT-600	Nanoparticles $D_{ext} \approx$ 15–45 nm	Anatase (highly crystalline) L_{hkl} = 18 nm	71	0.35	3.17
HTNT-700	Nanoparticles $D_{ext} \approx$ 30–70 nm	96% anatase, (highly crystalline) L_{hkl} = 32 nm 4% rutile L_{hkl} = 72 nm	30	0.16	2.94
HTNW	Nanowires	H$_2$Ti$_3$O$_5$·H$_2$O (poorly crystalline)	375	1.53	3.26
HTNW-700	Mixture of nanoplates and nanoparticles $D_{ext} \approx$ 10–40 nm, $L \approx$ 60–200 nm	Anatase (highly crystalline) L_{hkl} = 30 nm	50	0.31	3.04
TNR	Trounced nanorods $D_{ext} \approx$ 30–60 nm, $L \approx$ 100–200 nm	Anatase (highly crystalline) L_{hkl} = 47 nm	16	0.13	3.10
P25	Nanoparticles $D_{ext} \approx$ 20–30 nm	80% anatase, L_{hkl} = 19 nm 20% rutile L_{hkl} = 29 nm	50	0.18	3.20

D_{ext}: external diameter; D_{int}: internal diameter; L: length; L_{hkl}: crystallite size.
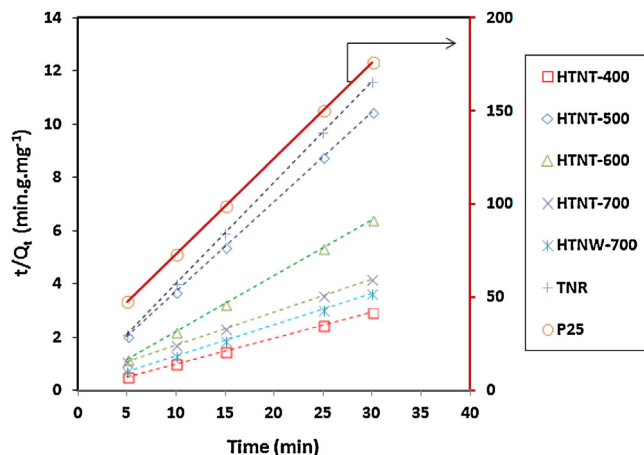
Fig. 4. Kinetics of adsorption of phenol on the elaborated TiO$_2$ nanomaterial surfaces.
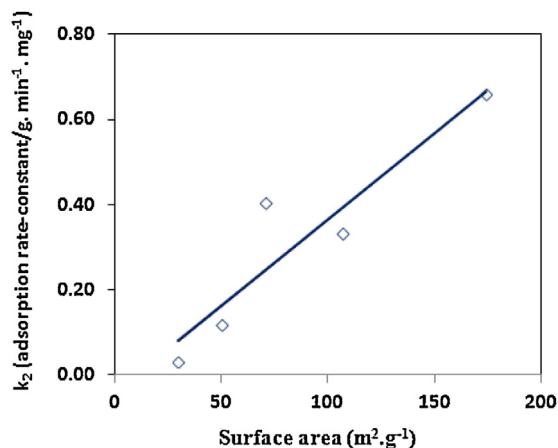
Fig. 5. Evolution of adsorption rate constant (k_2) as a function of specific surface area of TiO$_2$ nanomaterials.

3.2.2. Fit using the quasi-second-order kinetic model

The quasi-second-order kinetic model (Eq. (3)) is based on the assumption that the adsorption rate is determined by the square of the number of vacant adsorption sites on the surface of adsorbent [62].

$$\frac{dQ_t}{dt} = k_2 \cdot (Q_e - Q_t)^2 \qquad (3)$$

where Q_t and Q_e are the amounts of phenol at time t and at equilibrium (mg g^{-1}), respectively and k_2 is the quasi-second-order rate constant (g min^{-1} mg^{-1}). The integration of Eq. (3) gives:

$$\frac{t}{Q_t} = \frac{1}{k_2(Q_e)^2} + \frac{1}{Q_e}t \qquad (4)$$

Fig. 4 shows the variation of t/Q_t vs time for the different TiO$_2$ nanomaterials. Our data fits well to a quasi-second-order kinetics process; the coefficients of correlation R^2 are high (>0.99). The quasi-second-order rate constants (k_2) for the different materials are listed in Table 2. For HTNT materials, after post-thermal treatments (400–700 °C), the rate constant k_2 tends to decrease in a similar fashion with the variation of specific surface areas (Fig. 5) with a maximum k_2 value of 0.66 g min^{-1} mg^{-1} for HTNT-400 decreasing to a very low k_2 value of 0.03 g min^{-1} mg^{-1} for HTNT-700. In the case of HTNW-700, the rate constant k_2 remains quite low (0.12 g min^{-1} mg^{-1}) while a relatively high rate constant is obtained for TNR (0.64 g min^{-1} mg^{-1}). This value, similar to the one obtained for HTNT-400, is however surprising taking

Table 2
Adsorption characteristics of phenol in the dark and kinetic data of the phenol photocatalytic degradation in the presence of different TiO_2 nanomaterials.

	Dark			UV conditions	
	Q_{max} ($\mu mol\,g^{-1}$)	K_{obs} ($10^{-3}\,L\,\mu mol^{-1}$)	k_2 ($g\,min^{-1}\,mg^{-1}$)	k ($\mu mol\,L^{-1}\,min^{-1}$)	K_{UV} ($10^{-3}\,L\,\mu mol^{-1}$)
HTNT-400	0.79	27.4	0.66	1.25	9.6
HTNT-500	16.90	5.4	0.33	2.53	5.4
HTNT-600	89.34	0.6	0.40	3.27	13.1
HTNT-700	42.84	1.0	0.03	4.06	5.2
HTNW-700	1.72	5.3	0.12	4.23	19.1
TNR	35.11	3.4	0.64	5.80	4.02
P25	53.22	0.7	1.22	6.56	16.7

Q_{max}: maximum quantities of Ph adsorbed per gram of photocatalyst; K_{obs}: adsorption constants in the dark; k: rate constant of Ph photodegradation; K_{UV}: adsorption constants under the UV conditions, k_2 is the rate constant of the quasi-second-order ($g\,min^{-1}\,mg^{-1}$).
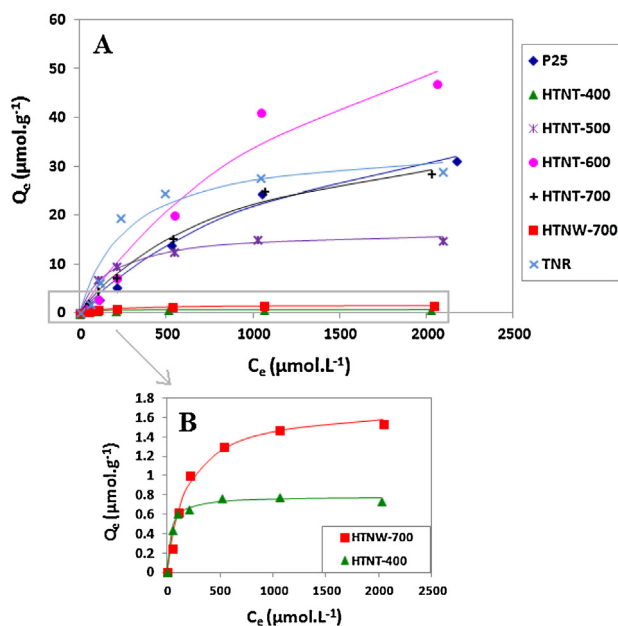
Fig. 6. Adsorption isotherms of phenol on the elaborated TiO_2 nanomaterial surfaces. Symbols refer to experiment values and curves to the Langmuir model.

into account the low surface area of TNR ($16\,m^2/g$ vs $174\,m^2/g$ for HTNT-400) showing that correlation between the rate constant k_2 and the surface area is only valid for 1D TiO_2 nanomaterials or for TiO_2 solids resulting from the calcination of 1D TiO_2 nanostructures. Finally, P25 shows the highest adsorption rate constant (k_2) with respect to HTNT and HTNW nanomaterials with a k_2 value of $1.22\,g\,min^{-1}\,mg^{-1}$.

The absence of correlation for TNR and P25 combined with their high k_2 values suggests that their structural properties (crystallite sizes, defects number and density) and textural properties differing from those observed with HTNT and HTNW nanomaterials. In nanorods, the surface-to-volume ratio is higher than that found in nanospheres, and this would guarantee a higher density of active sites available for surface reactions as well as high interfacial charge carrier transfer rate [63].

3.3. Phenol adsorption isotherms

The phenol adsorption equilibrium is reached within 30 min of contact time under magnetically stirred materials Phenol adsorption isotherms, in the dark, on the surface of elaborated TiO_2 nanomaterials and P25 are shown in Fig. 6A–B. From these curves, it can be deduced that all the phenol adsorption isotherms follow the Langmuir model (Eq. (5)) independently of the used sample:

$$Q_e = \frac{K_{obs}Q_{max}C_e}{1 + K_{obs}C_e} \tag{5}$$

where Q_e is the adsorbed quantity of phenol ($\mu mol\,g^{-1}$), C_e is the phenol concentration ($\mu mol\,L^{-1}$) at the adsorption equilibrium, K_{obs} is the adsorption constant in the dark ($L\,\mu mol^{-1}$) and Q_{max} is the maximum adsorbed quantity of phenol ($\mu mol\,g^{-1}$).

From the data in Fig. 6A–B, the adsorption constants (K_{obs}) and the maximum quantity of phenol (Q_{max}) adsorbed for each photocatalyst were determined by the method of the least squares fitting according to Eq. (5). These values are reported in Table 2. The maximum phenol adsorption in the dark Q_{max} decreased in the following order: HTNT-600 > P25 > HTNT-700 > TNR > HTNT-500 » HTNW-700 > HTNT-400.

In the case of HTNT materials, results revealed a very different evolution of Q_{max} and K_{obs} with the temperature of calcination compared to the rate constant k_2 in the preceding section. For Q_{max} values, a very low amount of phenol can be adsorbed on the HTNT-400 even if presenting the highest specific surface area among the different HTNT materials. This shows that the phenol adsorption capacity is not correlated with the variation in surface area. Increasing the temperature of calcination up to 600 °C leads to a very strong increase of the maximum amount of phenol to be adsorbed on the HTNT-600 solid ($89.3\,\mu mol\,g^{-1}$) while a further increase of the temperature of calcination to 700 °C leads to a decrease of the amount adsorbed to $42.8\,\mu mol\,g^{-1}$. This result suggests that an increase of the crystallinity degree of HTNT materials results in a better phenol adsorption capacity. A similar conclusion can be reached concerning the highly crystalline TNR sample. By contrast, calcination of TiO_2 nanowires does not result in any significant adsorption of phenol on the surface of the HTNW-700 material. Finally, P25 presents a relatively high adsorption capacity of $53.2\,\mu mol\,g^{-1}$.

Determination of K_{obs} shows, on the opposite, a strong decrease of the adsorption constant values with the temperature of calcination of HTNT materials with a remarkable high K_{obs} value of $27.4 \times 10^{-3}\,L\,\mu mol^{-1}$ for HTNT-400. K_{obs} values meanwhile decrease strongly for further increase of the temperature of calcination. HTNW-700 and TNR show moderate K_{obs} values while P25 exhibits a very low adsorption constant.

Combining these observations with those found for the rate constant k_2, it can be concluded that the adsorption kinetics on HTNT-400 is relatively fast but also leads to a rapid surface saturation at low amount of phenol adsorbed. This was confirmed by the shape of the adsorption isotherm of HTNT-400 as shown in Fig. 6B. On the opposite, HTNT-600 and 700 are able to adsorb much larger amount of phenol but these materials are also slow to be surface saturated. A similar observation can be made for P25 with an even slower tendency to be surface-saturated. TNR and HTNT-500 present intermediate situations while HTNW-700 presents both a slow surface saturation and a low adsorption capacity.
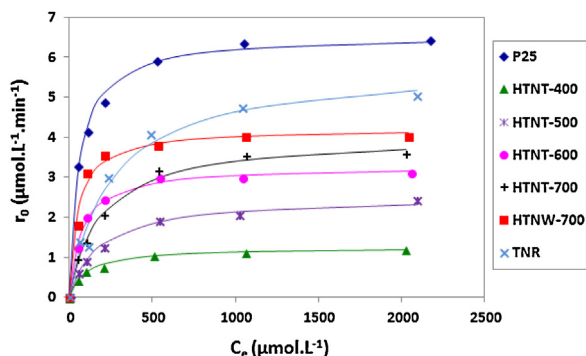
Fig. 7. Kinetics of photocatalytic degradation of phenol in the presence of elaborated TiO$_2$ nanomaterials. Comparison is provided with the P25 reference. Symbols refer to experiment values and curves to the Langmuir-Hinshelwood model.
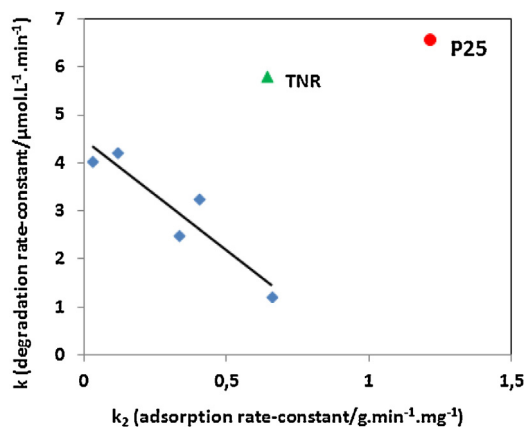

Fig. 8. Evolution of The phenol photodegradation rate constant (k) under UV as a function of the adsorption rate constant in the dark (k_2) for different TiO$_2$ nanomaterials.

3.4. Phenol photodegradation kinetics

After having determined the kinetics of phenol adsorption in the dark, the following paragraph will consider the kinetics results obtained during the photodegradation of phenol under UV conditions. At this stage, it is important to note that the as-elaborated and uncalcined materials (named HTNT and HTNW) are inactive under UV.

The evolution of the initial disappearance rate of phenol (r_0) represented as a function of the concentration of phenol at equilibrium (C_e) is reported in Fig. 7. Results reveal that below 10 mg L^{-1} ($\approx$106 μmol L^{-1}), the initial rate is proportional to the phenol concentration in solution (Eq. (6)) and reaches a plateau for higher concentrations. This type of curve can be modelized by a Langmuir–Hinshelwood (L–H) model (Eq. (7)) and are in good agreement with those reported for the degradation of several other organic compounds [43,64–66].

$$r_0 = kK_{UV}C_e \tag{6}$$

$$r_0 = \frac{kK_{UV}C_e}{1 + K_{UV}C_e} \tag{7}$$

with r_0 is the initial disappearance rate of phenol (μmol L^{-1} min^{-1}), k the rate constant of the reaction (μmol L^{-1} min^{-1}), K_{UV} the adsorption constant under UV conditions (L μmol^{-1}), and C_e the phenol concentration at the adsorption equilibrium (μmol L^{-1}).

The rate constant k and the adsorption constant K_{UV} under UV conditions are determined from Fig. 7 and reported in Table 2.

The evolution of the rate constant k and of the adsorption constant K_{UV} under UV conditions differs significantly to what was observed under dark conditions. In the case of the HTNT materials, increasing the calcination temperature from 400 °C to 700 °C leads to a steady increase of the rate constant k from 1.25 μmol L^{-1} min^{-1} for HTNT-400 to 4.06 μmol L^{-1} min^{-1} for HTNT-700. This evolution differs strikingly from the variation of the phenol adsorption capacity of each solid as determined from Q_{max} and K_{obs} values. Results in fact suggest a link between the tendency to surface saturation by phenol and the ability to photocatalyze this pollutant, i.e the faster the solid is surface saturated by phenol, the lower the photocatalytic activity is. Indeed, HTNT-400 tends to be saturated rapidly in phenol and this has for consequences a lower rate constant k value (1.25 μmol L^{-1} min^{-1}). However, with the increase of the calcination temperature, saturation becomes less and less fast resulting in a higher photocatalytic rate constant k. This result suggests a self-inhibition of the reaction by the phenol reactant. Similar observations can be made considering TNR and HTNW-700 with intermediate surface saturations. Finally, P25 with the slowest surface saturation corresponds to the highest rate constant k (6.56 μmol L^{-1} min^{-1}). The fact that the photocatalytic activity

tends to increase with a lower tendency to surface saturation can also be better ascertained by reporting the evolution of the rate constant k under UV conditions in function of the rate constant k_2 of phenol adsorption under dark conditions. An inverse correlation between k and k_2 is found for all the photocatalysts studied (Fig. 8) except P25 showing the coverage rate (θ) will vary simultaneously with the adsorption rate k_2. Therefore, higher photocatalytic activity is achieved for low surface coverage rate (or low adsorption rate k_2). In addition, for 1-D nanostructured nanorods the space charge region is well constructed along the longitudinal direction of TiO$_2$ nanocrystal, meaning that photogenerated electrons can flow in the direction of the crystal length. Increased delocalization of electrons at 1-D nanostructured crystals can lead to a remarkable decrease in e−/h+ recombination probability. Consequently, larger numbers of e− and h+ exist on the active sites of the surface, resulting in higher activity compared with spherical nanoparticles. Joo et al. [67] reported that TiO$_2$ nanorods have superior photocatalytic inactivation of E. coli compared with Degussa P25 99% of the E. coli was inactivated after 92 and 140 min by TiO$_2$ nanorods and P25, respectively. Herein, the highly crystalline TNR material shows a good activity in the photodegradation of phenol with respect to nanowires (HTNW-700) and nanoparticles (HTNT-700). The photocatalytic activity vary in the order P25 > TNR > HTNW-700 ≈ HTNT-700 (Table 2). P25 represents a notable exception with both high k_2 and k values. The activity of the two polymorphs for the photocatalytic oxidation of phenol in water was examined [68]. It was shown that the rutile phase (39 m^2 g^{-1}) initially decomposed phenol much faster and follows a first-order process reasonably well ($k = 4 \times 10^{-5}$ s^{-1}). The photodecomposition process using the anatase phase led, however, to a much more rapid overall degradation following an initial slower rate of phenol oxidation. The results indicate that the observed difference of the photodecomposition process for the two TiO$_2$ phases is due to the formation of different intermediates in good agreement with our results. Herein, the activity of P25 and HNTW-700 are respectively 6.5 × 10^{-3} s^{-1} and 4 × 10^{-3} s^{-1} are much higher compared to pure rutile phase. The low activity of rutile phase is attributed to its higher electron-hole recombination rate. Although, TiO$_2$ anatase has attracted a great deal in photocatalysis; various parameters were examined (such as: the effects of adsorption, temperature, intensity of light, pH, and the presence of anions, cations); few studies have been focused on the influence of titanium oxide morphology and structure. Herein, HTNW (nanowires) shows similar textural properties as commercial TiO2 P25 (80% anatase). The photodegradation activities of phenol over rutile phase resp. HNTW (anatase) are 4 × 10^{-5} s^{-1} resp. 4 × 10^{-3} s^{-1}. Therefore the

photocatalytic contribution of rutile phase (around 20%) in P25 might be neglected.

3.5. Intermediates and mechanism

HTNW-700 and P25 nanomaterials having a similar specific surface area (ca. 50 $m^2 g^{-1}$) and interesting photocatalytic activities in phenol degradation were selected for the mineralization study. Initial phenol concentration of 10 mg L^{-1} (106 μmol L^{-1}) was chosen at natural pH.

The conversion of phenol obtained using P25 is higher than the one obtained using HTNW-700 all along the photocatalytic test. Complete degradation of phenol is reached after 60 min in the case of P25 and after ca. 360 min in the case of HTNW-700 (Supplementary data Fig. S2-A). both materials achieve a mineralization of ca. 95% after 360 min. Using P25, at the beginning of the photocatalytic degradation of phenol, mineralization is fast until about 60 min of reaction and then slowed down. In the case of HTNW-700, mineralization is slower than for P25 and beyond 180 min of reaction the same rate of mineralization is observed for both materials (Supplementary data Fig. S2-B).

The evolution of TOC (measured TOC) and of organic carbon deriving from residual phenol in solution (phenol residual OC) over P25 and HTNW-700 photocatalysts are represented in Fig. 9. Difference between these two curves reflects the presence of several intermediates compounds which are not completely degraded into CO_2 (intermediates OC). The disappearance of phenolic molecules (106 μmol L^{-1}, natural pH) and the appearance of the intermediates compounds were then followed by HPLC in the presence of P25 and HTNW-700 as photocatalysts. Main intermediates products detected by HPLC are listed in Supplementary data Table T1 with their corresponding retention times.

The identification and quantification of the intermediates products may help in proposing a formal reaction mechanism scheme for the phenol degradation using P25/UV-A or HTNW-700/UV-A systems (Supplementary data Fig. S3). Propionic acid appears in the solution in higher amount than the other intermediates; this is probably due to the conversion of the majority of the aromatic products (hydroquinone, catechol, and 1,4-benzoquinone) formed during the degradation of phenol into propionic acid. However, using P25/UV-A (Supplementary data Fig. S3-A), more intermediates products were identified than when using HTNW-700. These intermediates are mainly aromatic compounds 'hydroquinone (Hyd), catechol (Cat) and 1,4-benzoquinone (Bzq)) and also carboxylic acids 'maleic acid (MA), fumaric acid (FuA), succinic acid (SA), tartaric acid (TA), propionic acid (PA), acetic acid (AA), and formic acid (FA)). A reaction time of 40 min under UV-A illumination is sufficient to reach the maximum formation of hydroquinone, succinic acid, propionic acid, and acetic acid. Those intermediates are fully degraded later while the maximum formation of 1,4-benzoquinone, tartaric acid and formic acid is reached faster (after only 15 min). Only small amounts of catechol, maleic acid, and fumaric acid were detected mainly at the beginning of the reaction suggesting their fast initial consumption. On the other hand, using HTNW-700 (Supplementary data Fig. S3-B) leads mainly to three intermediates compounds namely: hydroquinone, propionic acid and a low proportion of 1,4 benzoquinone. The concentrations of these intermediates reach a maximum after 100 min of UV-A illumination. Beyond this time, full degradation is observed.

The evolution of the total conversion of phenol (or TTG) and of the yield (or TTI) of each product (Eq. (10)) (except CO_2) is reported in Fig. 10:

$$TTI = \frac{[Int]_t}{[Ph]_0} \tag{10}$$

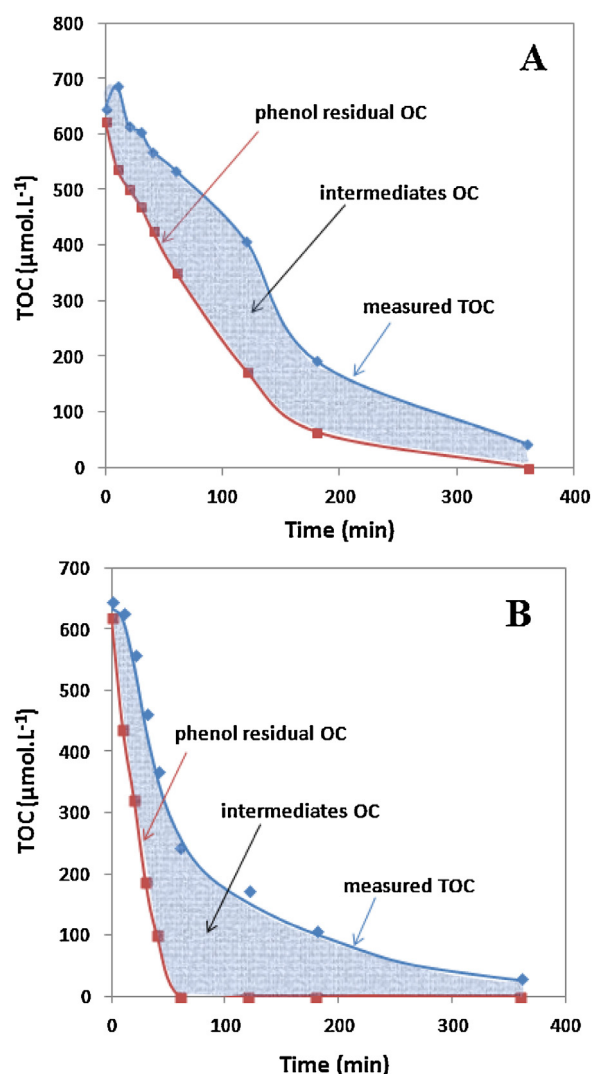**Fig. 9.** Evolution of total organic carbon in the degradation of 10 mg L^{-1} ($\approx$106 μmol L^{-1}) of phenol using HTNW-700 (A) and P25 (B).
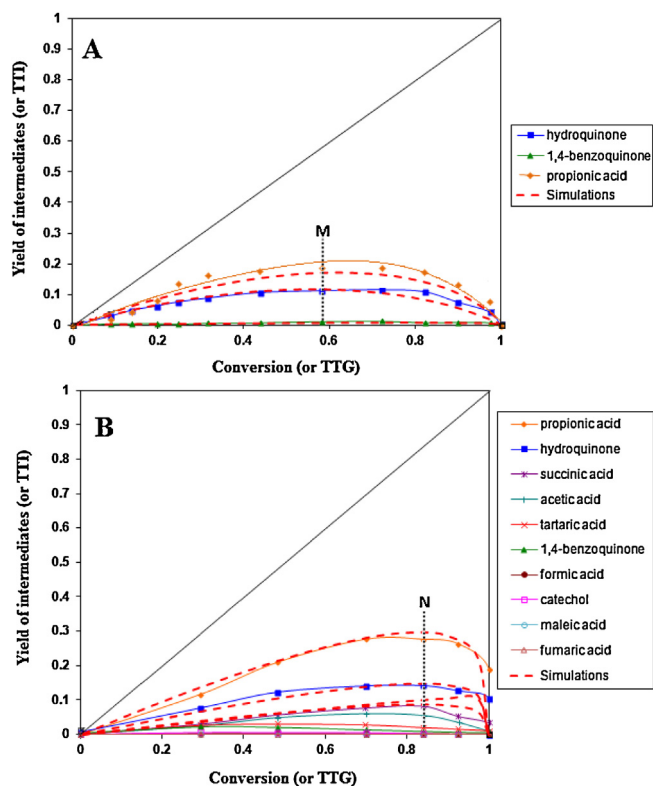
where $[Ph]_0$ corresponds to the initial concentration of phenol and $[Int]_t$ (μmol L^{-1}) to the concentration of an intermediate compound at time t.

Based on the results reported in Fig. 10, selectivity was determined for each product at a conversion rate of 40% (Fig. S4 supplementary information).

Over P25, the photocatalytic degradation of phenol favors the formation of propionic acid (33%) at the expense of other carboxylic acids which are formed in lower proportions (mainly succinic acid: 10% and acetic acid: 6.6%) while only hydroquinone is formed in significant amounts among the aromatic compounds (17%). Over HTNW-700, the same behavior is observed but with an even higher selectivity to propionic acid (52%) while no other carboxylic acids can be detected. Similarly, hydroquinone is also formed in higher proportion (28%).

Starting from these observations, it can be concluded that the photocatalytic degradation of phenol by both P25/UV-A and HTNW-700/UV-A systems follows the same reaction mechanism but using HTNW-700 leads to a slower phenol photodegradation than using P25. These results could be explained by the low rate constants of photodegradation of by-products (propionic acid, hydroquinone and 1,4-benzoquinone). However, we must also consider the degradation of the low molecular weight carboxylic acids formed during the reaction like formic acid. Indeed, apart from

Fig. 10. Representative curves of conversion rate of intermediate products (TTI) as a function of the total conversion percentage of phenol (TTG) using HTNW-700/UV-A (A) and P25/UV-A (B) photocatalytic systems. The continuous lines are related to the experimental results and the dashed lines are related to the simulations.

Table 3
Kinetic constants of intermediate reactions for both HTNW-700/UV-A and P25/UV-A photocatalytic systems.

HTNW-700/UV-A		P25/UV-A	
k_1 (min^{-1})	0.24	k'_1 (min^{-1})	0.39
k_2 (min^{-1})	0.40 k_1	k'_2 (min^{-1})	0.14 k'_1
k_3 (min^{-1})	1.06 k_1	k'_3 (min^{-1})	1.00 k'_1
k_4 (min^{-1})	0.45 k_1	k'_4 (min^{-1})	1.17 k'_1
k_5 (min^{-1})	1.07 k_1	k'_5 (min^{-1})	0.28 k'_1
		k'_6 (min^{-1})	0.29 k'_1
		k'_7 (min^{-1})	0.07 k'_1

$$\frac{d(TT_{PA})}{dt} = k_3 TT_{Hyd} + k_4 TT_{Bzq} - k_5 TT_{PA} \tag{14}$$

Moreover, kinetic Eqs. (15)–(17) can be solved at point M (conversion: 58%) (cf. Fig. 10A) for which the different yield curves reach maxima:

$$\frac{dTT_{Hyd}}{dTTG} = 1 - \frac{k_2 + k_3}{k_1} \cdot \frac{TT_{Hyd}}{(1 - TTG)} \tag{15}$$

$$\frac{dTT_{Bzq}}{dTTG} = \frac{k_2}{k_1} \cdot \frac{TT_{Hyd}}{(1 - TTG)} - \frac{k_4}{k_1} \cdot \frac{TT_{Bzq}}{(1 - TTG)} \tag{16}$$

$$\frac{dTT_{PA}}{dTTG} = \frac{k_3}{k_1} \cdot \frac{TT_{Hyd}}{(1 - TTG)} + \frac{k_4}{k_1} \cdot \frac{TT_{Bzq}}{(1 - TTG)} - \frac{k_5}{k_1} \cdot \frac{TT_{PA}}{(1 - TTG)} \tag{17}$$

Following the same methodology, the following kinetic constants were determined for the P25/UV-A system (Eqs. (18)–(22)) considering the point N (conversion: 83%) (cf. Fig. 10B):

$$\frac{dTT_{Hyd}}{dTTG} = 1 - \frac{k'_2 + k'_3}{k'_1} \cdot \frac{TT_{Hyd}}{(1 - TTG)} \tag{18}$$

$$\frac{dTT_{Bzq}}{dTTG} = \frac{k'_2}{k'_1} \cdot \frac{TT_{Hyd}}{(1 - TTG)} - \frac{k'_4}{k'_1} \cdot \frac{TT_{Bzq}}{(1 - TTG)} \tag{19}$$

$$\frac{dTT_{AS}}{dTTG} = \frac{k'_3}{k'_1} \cdot \frac{TT_{Hyd}}{(1 - TTG)} + \frac{k'_4}{k'_1} \cdot \frac{TT_{Bzq}}{(1 - TTG)} - \frac{k'_5}{k'_1} \cdot \frac{TT_{AS}}{(1 - TTG)} \tag{20}$$

$$\frac{dTT_{AP}}{dTTG} = \frac{k'_5}{k'_1} \cdot \frac{TT_{AS}}{(1 - TTG)} - \frac{k'_6}{k'_1} \cdot \frac{TT_{AP}}{(1 - TTG)} \tag{21}$$

$$\frac{dTT_{AA}}{dTTG} = \frac{k'_6}{k'_1} \cdot \frac{TT_{AP}}{(1 - TTG)} - \frac{k'_7}{k'_1} \cdot \frac{TT_{AA}}{(1 - TTG)} \tag{22}$$

Table 3 summarizes the different kinetic pseudo-rate constants determined for both HTNW-700 and P25. Based on the integration of the kinetic equations described above, a simulations of the experimental curves (yield vs conversion) were plotted in Fig. 10 showing a good agreement between experimental and simulated curves.

In the case of HTNW-700, the calculation of the rate constants reported in Table 3 shows a relatively slow transformation of hydroquinone into benzoquinone while the propionic acid formation is faster (mainly from hydroquinone) than its consumption into CO$_x$. These results explain that the photocatalytic degradation of phenol onto HTNW-700 led almost only to hydroquinone and propionic acid.

In the case of P25, the transformation of hydroquinone into benzoquinone is even slower than for HTNW-700 while the formation of succinic acid from both hydroquinone and benzoquinone is quite rapid. However, the degradation of succinic acid into lower molecular weight carboxylic acids is quite low explaining here the detection of not only hydroquinone and propionic acid as products of the phenol degradation but also of different lower molecular weight carboxylic acids like succinic acid and acetic acid.

propionic acid, the absence of all other carboxylic acids among the products obtained by degradation of phenol over HTNW-700 suggests a higher photocatalytic activity of this nanomaterials towards the degradation of low molecular weight carboxylic acids than over P25. This result is in agreement with our previous study [48] for which HTNW-700 was found to be twice more active for the photocatalytic degradation of formic acid than P25. The lower photocatalytic degradation of phenol over HTNW-700 would then result from a competition for adsorption between phenol and some of its by-products on photocatalytic active sites. This result would be in agreement with our previous observations showing a lower tendency to degrade phenol with a higher tendency to saturate the surface of the photocatalysts with the reactant. This initial low degradation rate of phenol into mainly carboxylic acids would result in a self poisoning of the surface by the reactant. A significant photocatalytic activity would then only be maintained through the ability of the nanomaterial avoiding a complete surface saturation by phenol pathways.

Based on the as-formed intermediates and selectivity results, two reaction schemes are proposed for HTNW-700/UV-A (Fig. 11A) and P25/UV-A (Fig. 11B), respectively. For simplification purposes, the oxidation of each intermediate is considered to follow pseudo-first order kinetics.

Using the reaction scheme described in Fig. 11A, the following kinetic equations can be written (Eqs (11)–(14)):

$$-\frac{d(1 - TTG)}{dt} = k_1(1 - TTG) \tag{11}$$

$$\frac{d(TT_{Hyd})}{dt} = k_1(1 - TTG) - (k_2 + k_3)TT_{Hyd} \tag{12}$$

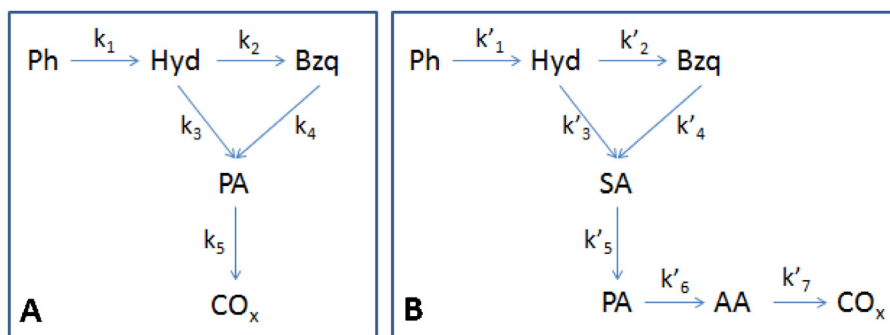$$\frac{d(TT_{Bzq})}{dt} = k_2 TT_{Hyd} - k_4 TT_{Bzq} \tag{13}$$

Fig. 11. Proposed formal kinetic schemes for the photocatalytic degradation of phenol using HTNW-700/UV-A (A) and P25/UV-A (B) nanomaterials, respectively.

4. Conclusions

TiO$_2$ anatase nanomaterials with controlled textural, structural and morphological properties (nanotubes, nanowires, nanorods, and nanospheres) have been evaluated in the phenol photocatalytic degradation. Control of the elaboration routes of various TiO$_2$ photocatalysts was performed by tuning simultaneously the surface/bulk defects, the crystallite size and the specific surface area.

Results show that the phenol kinetics adsorption process follows a quasi-second-order reaction model. Analysis of the rate constants and adsorption constants for the phenol adsorption in the dark and of the rate constant for the photodegradation of phenol under UV conditions suggests a self-inhibition process by the phenol reactant during the photocatalytic degradation of this pollutant which can only be counterbalanced by the maintaining of a portion of the photocatalyst surface free from phenol adsorption. This can be obtained only through calcination at high temperature (up to 700 °C) of HTNT and HTNW materials or through hydrothermal treatment in deionized water leading to the TNR nanomaterial. However, even if gain in photocatalytic activity was significantly obtained, P25 still performs better than pure anatase TiO$_2$ solids. Selectivity results as well as calculation of kinetic rate constants for the respective reaction schemes for the degradation of phenol over HTNW-700 and P25 also confirm a faster transformation of intermediates like propionic acid over HTNW-700 than over P25 favoring an even higher saturation by phenol of HTNW-700 compared to P25.

Acknowledgments

Appendix A. Supplementary data

Supplementary material related to this article can be found, in the online version, at http://dx.doi.org/10.1016/j.apcatb.2014.08.010.

References

[1] R. Zonta, M. Botter, D. Cassin, R. Pini, M. Scattolin, L. Zaggia, Mar. Pollut. Bull. 55 (2007) 529–542.
[2] A.K. Krishna, M. Satyanarayanan, P.K. Govil, J. Hazard. Mater. 167 (2009) 366–373.
[3] R.C. Martínez, E.R. Gonzalo, M.E.F. Laespada, F.J.S. San Román, J. Chromatogr. A 869 (2000) 471–480.
[4] S. Savci, APCBEE Procedia 1 (2012) 287–292.
[5] T. Zabel, I. Milne, G. Mckay, Urban Water 3 (2001) 25–32.
[6] I. Gnecco, C. Berretta, L.G. Lanza, P. La Barbera, Atmos. Res. 77 (2005) 60–73.
[7] A. Sonune, R. Ghate, Desalination 167 (2004) 55–63.
[8] H. Hyung, J.-H. Kim, Water Res. 43 (2009) 2463–2470.
[9] W. Schussler, L. Nitschke, Water Res. 33 (1999) 2884–2887.
[10] M. Ma, K. Rao, Z. Wang, Environ. Pollut. 147 (2007) 331–336.
[11] R. Törnqvist, J. Jarsjö, B. Karimov, Environ. Int. 37 (2011) 435–442.
[12] R. Andreozzi, V. Caprio, A. Insola, R. Marotta, Catal. Today 53 (1999) 51–59.
[13] R. Bauer, G. Waldner, H. Fallmann, S. Hager, M. Klare, T. Krutzler, S. Malato, P. Maletzky, Catal. Today 53 (1999) 131–144.
[14] A. Matilainen, M. Sillanpää, Chemosphere 80 (2010) 351–365.
[15] I. Oller, S. Malato, J.A. Sánchez-Pérez, Sci. Total Environ. 409 (2011) 4141–4166.
[16] J.-M. Herrmann, Catal. Today 53 (1999) 115–129.
[17] J. Araña, J.A. Herrera Melián, J.M. Doña Rodríguez, O. González Díaz, A. Viera, J. Pérez Peña, P.M. Marrero Sosa, V. Espino Jiménez, Catal. Today 76 (2002) 279–289.
[18] S. Malato Rodríguez, J. Blanco Gálvez, M.I. Maldonado Rubio, P. Fernández Ibáñez, W. Gernjak, I. Oller Alberola, Chemosphere 58 (2005) 391–398.
[19] A. Mills, S. Le Hunte, J. Photochem. Photobiol. A 108 (1997) 1–35.
[20] E. Pelizzetti, C. Minero, Colloid Surf. A 151 (1999) 321–327.
[21] C. Karunakaran, R. Dhanalakshmi, Sol. Energy Mater. Sol. C 92 (2008) 1315–1321.
[22] E. Pelizzetti, C. Minero, Electrochim. Acta 38 (1993) 47–55.
[23] K. Hashimoto, H. Irie, A. Fujishima, Jpn. J. Appl. Phys. 44 (2005) 8269–8285.
[24] U.I. Gaya, A.H. Abdullah, J. Photochem. Photobiol. C: Photochem. Rev. 9 (2008) 1–12.
[25] M. Halmann, A.J. Hunt, D. Spath, Sol. Energy Mater. Sol. C 26 (1992) 1–16.
[26] Y. Ku, R.-M. Leu, K.-C. Lee, Water Res. 30 (1996) 2569–2578.
[27] J.C. Crittenden, J. Liu, D.W. Hand, D.L. Perram, Water Res. 31 (1997) 429–438.
[28] I. Mazzarino, P. Piccinini, Chem. Eng. Sci. 54 (1999) 3107–3111.
[29] A. Assabane, Y. Ait Ichou, H. Tahiri, C. Guillard, J.-M. Herrmann, Appl. Catal. B: Environ. 24 (2000) 71–87.
[30] D. Vione, C. Minero, V. Maurino, M.E. Carlotti, T. Picatonotto, E. Pelizzetti, Appl. Catal. B: Environ. 58 (2005) 79–88.
[31] A. Marinas, C. Guillard, J.M. Marinas, A. Fernández-Alba, A. Aguëra, J.-M. Herrmann, Appl. Catal. B: Environ. 34 (2001) 241–252.
[32] M. Carrier, N. Perol, J.-M. Herrmann, C. Bordes, S. Horikoshi, J.O. Paisse, R. Baudot, C. Guillard, Appl. Catal. B: Environ. 65 (2006) 11–20.
[33] C. Guillard, H. Lachheb, A. Houas, M. Ksibi, E. Elaloui, J.-M. Herrmann, J. Photochem. Photobiol. A 158 (2003) 27–36.
[34] S. Lathasree, A. Nageswara Rao, B. SivaSankar, V. Sadasivam, K. Rengaraj, J. Mol. Catal. A: Chem. 223 (2004) 101–105.
[35] N. Kashif, F. Ouyang, J. Environ. Sci. 21 (2009) 527–533.
[36] S.-S. Hong, C.-S. Ju, C.-G. Lim, B.-H. Ahn, K.-T. Lim, G.-D. Lee, J. Ind. Eng. Chem. 7 (2001) 99–104.
[37] Z. Guo, R. Ma, G. Li, Chem. Eng. J. 119 (2006) 55–59.
[38] J. Araña, J.M. Doña-Rodríguez, D. Portillo-Carrizo, C. Fernández-Rodríguez, J. Pérez-Peña, O. González Díaz, J.A. Navío, M. Macías, Appl. Catal. B: Environ. 100 (2010) 346–354.
[39] S. Ahmed, M.G. Rasul, W.N. Martens, R. Brown, M.A. Hashib, Desalination 261 (2010) 3–18.
[40] G. Busca, S. Berardinelli, C. Resini, L. Arrigi, J. Hazard. Mater. 160 (2008) 265–288.
[41] L.F. Liotta, M. Gruttadauria, G. Di Carlo, G. Perrini, V. Librando, J. Hazard. Mater. 162 (2009) 588–606.
[42] C. Renzi, C. Guillard, J.-M. Herrmann, P. Pichat, G. Baldi, Chemosphere 35 (1997) 819–826.
[43] C.-H. Chiou, C.-Y. Wu, R.-S. Juang, Chem. Eng. J. 139 (2008) 322–329.
[44] A.K. Datye, G. Riegel, J.R. Bolton, M. Huang, M.R. Prairie, J. Solid State Chem. 115 (1995) 236–239.
[45] T. Ohno, K. Sarukawa, K. Tokieda, M. Matsumura, J. Catal. 203 (2001) 82–86.
[46] J.A. Toledo Antonio, M.A. Cortes-Jacome, S.L. Orozco-Cerros, E. Montiel-Palacios, R. Suarez-Parra, C. Angeles-Chavez, J. Navarete, E. López-Salinas, Appl. Catal. B: Environ. 100 (2011) 47–54.

[47] X.-Q. Gong, A. Selloni, J. Catal. 249 (2007) 134–139.
[48] S. Liu, N. Jaffrezic, C. Guillard, Appl. Surf. Sci. 255 (2008) 2704–2709.
[49] K. Nakata, A. Fujishima, J. Photochem. Photobiol. C: Photochem. Rev. 13 (2012) 169–189.
[50] A. Turki, H. Kochkar, C. Guillard, G. Berhault, A. Ghorbel, App. Catal. B: Environ. 138–139 (2013) 401–415.
[51] H. Kochkar, N. Lakhdhar, G. Berhault, M. Bausach, A. Ghorbel, J. Phys. Chem. C 113 (2009) 1672–1679.
[52] A. Turki, H. Kochkar, I. García-Fernández, M.I. Polo-López, A. Ghorbel, C. Guillard, G. Berhault, P. Fernández-Ibáñez, Catal. Today 209 (2013) 47–152.
[53] A. Turki, F. Dappozze, C. Guillard, G. Berhault, Z. Ksibi, H. Kochkar, J. Photochem. Photobiol. A: Chem. 279 (2014) 8–16.
[54] J. Jitputti, Y. Suzuki, S. Yoshikawa, Catal. Commun. 9 (2008) 1265–1271.
[55] H. Peng, X. Wang, G. Li, H. Pang, X. Chen, Mater. Lett. 64 (2010) 1898–1901.
[56] J. Li, Y. Yu, Q. Chen, J. Li, D. Xu, Cryst. Growth Des. 10 (2010) 2111–2115.
[57] S. Mozia, E. Borowiak-Paleń, J. Przepiórski, B. Grzmil, T. Tsumura, M. Toyoda, J. Grzechulska-Damszel, A.W. Morawski, J. Phys. Chem. Solids 71 (2010) 263–272.
[58] B. Vijayan, N.M. Dimitrijevic, T. Rajh, K. Gray, J. Phys. Chem. C 114 (2010) 12994–13002.
[59] J.A. Toledo-Antonio, S. Capula, M.A. Cortés-Jácome, C. Angeles-Chávez, E. López-Salinas, G. Ferrat, J. Navarrete, J. Escobar, J. Phys. Chem. C 111 (2007) 10799–10805.
[60] J.A. Toledo-Antonio, M.A. Cortés-Jácome, J. Navarrete, C. Angeles-Chávez, E. López-Salinas, A. Rendon-Rivera, Catal. Today 155 (2010) 247–254.
[61] S. Lagergren, Zur theorie der sogenannten adsorption gelöster stoffe, Kungliga Svenska Vetenskapsakademiens, Handlingar 24 (1898) 1–39.
[62] G. Blanchard, M. Maunaye, G. Martin, Water Res. 18 (1984) 1501–1507.
[63] B. Wang, D. Xue, Y. Shi, F. Xue, in: W.V. Prescott, A.I. Schwartz (Eds.), Nanorods, Nanotubes and Nanomaterials Research Progress, New Nova Science, New York, NY, USA, 2008, pp. 163–201.
[64] R.W. Matthews, J. Catal. 111 (1988) 264–272.
[65] S. Valencia, F. Cataño, L. Rios, G. Restrepo, J. Marín, Appl. Catal. B: Environ. 104 (2011) 300–304.
[66] L. Elsellami, F. Vocanson, F. Dappozze, R. Baudot, G. Febvay, M. Rey, A. Houas, C. Guillard, Appl. Catal. B: Environ. 94 (2010) 192–199.
[67] J. Joo, S.G. Kwon, T. Yu, M. Cho, J. Lee, J. Yoon, T. Hyeon, J. Phys. Chem. B 109 (2005) 15297–15302.
[68] M. Andersson, L. Österlund, S. Ljungström, A. Palmqvist, J. Phys. Chem. B 106 (2002) 10674–10679.